AMERICAN SOCIETY FOR MICROBIOLOGY | Journal of Virology®

STRUCTURE AND ASSEMBLY

Molecular Characterization of the Viroporin Function of Foot-and-Mouth Disease Virus Nonstructural Protein 2B

D. P. Gladue,[a] E. Largo,[b,c] I. de la Arada,[b,c] V. M. Aguilella,[d] A. Alcaraz,[d] J. L. R. Arrondo,[b,c] L. G. Holinka,[a] E. Brocchi,[e] E. Ramirez-Medina,[a] E. A. Vuono,[a] K. A. Berggren,[a] C. Carrillo,[f] J. L. Nieva,[b,c] M. V. Borca[a]

[a]Plum Island Animal Disease Center, ARS, USDA, Greenport, New York, USA
[b]Biofisika Institute (CSIC-UPV/EHU), University of the Basque Country, Bilbao, Spain
[c]Department of Biochemistry and Molecular Biology, University of the Basque Country, Bilbao, Spain
[d]Laboratory of Molecular Biophysics, Department of Physics, University Jaume I, Castellón de la Plana, Spain
[e]Istituto Zooprofilattico Sperimentale della Lombardia e dell'Emilia Romagna, Brescia, Italy
[f]Plum Island Animal Disease Center, APHIS, USDA, Greenport, New York, USA

ABSTRACT Nonstructural protein 2B of foot-and-mouth disease (FMD) virus (FMDV) is comprised of a small, hydrophobic, 154-amino-acid protein. Structure-function analyses demonstrated that FMDV 2B is an ion channel-forming protein. Infrared spectroscopy measurements using partially overlapping peptides that spanned regions between amino acids 28 and 147 demonstrated the adoption of helical conformations in two putative transmembrane regions between residues 60 and 78 and between residues 119 and 147 and a third transmembrane region between residues 79 and 106, adopting a mainly extended structure. Using synthetic peptides, ion channel activity measurements in planar lipid bilayers and imaging of single giant unilamellar vesicles (GUVs) revealed the existence of two sequences endowed with membrane-porating activity: one spanning FMDV 2B residues 55 to 82 and the other spanning the C-terminal region of 2B from residues 99 to 147. Mapping the latter sequence identified residues 119 to 147 as being responsible for the activity. Experiments to assess the degree of insertion of the synthetic peptides in bilayers and the inclination angle adopted by each peptide regarding the membrane plane normal confirm that residues 55 to 82 and 119 to 147 of 2B actively insert as transmembrane helices. Using reverse genetics, a panel of 13 FMD recombinant mutant viruses was designed, which harbored nonconservative as well as alanine substitutions in critical amino acid residues in the area between amino acid residues 28 and 147. Alterations to any of these structures interfered with pore channel activity and the capacity of the protein to permeabilize the endoplasmic reticulum (ER) to calcium and were lethal for virus replication. Thus, FMDV 2B emerges as the first member of the viroporin family containing two distinct pore domains.

IMPORTANCE FMDV nonstructural protein 2B is able to insert itself into cellular membranes to form a pore. This pore allows the passage of ions and small molecules through the membrane. In this study, we were able to show that both current and small molecules are able to pass though the pore made by 2B. We also discovered for the first time a virus with a pore-forming protein that contains two independent functional pores. By making mutations in our infectious clone of FMDV, we determined that mutations in either pore resulted in nonviable virus. This suggests that both pore-forming functions are independently required during FMDV infection.

KEYWORDS 2B, FMD, FMDV, viroporin, foot-and-mouth disease

Received 9 August 2018 **Accepted** 7 September 2018

Accepted manuscript posted online 19 September 2018

Citation Gladue DP, Largo E, de la Arada I, Aguilella VM, Alcaraz A, Arrondo JLR, Holinka LG, Brocchi E, Ramirez-Medina E, Vuono EA, Berggren KA, Carrillo C, Nieva JL, Borca MV. 2018. Molecular characterization of the viroporin function of foot-and-mouth disease virus nonstructural protein 2B. J Virol 92:e01360-18. https://doi.org/10.1128/JVI.01360-18.

Editor Julie K. Pfeiffer, University of Texas Southwestern Medical Center

Address correspondence to M. V. Borca, manuel.borca@ars.usda.gov.

D.P.G. and E.L. contributed equally to this article.

Foot-and-mouth disease (FMD) virus (FMDV), a single-stranded, positive RNA virus with a genome of approximately 8,500 bases, belongs to the *Aphthovirus* genus of the *Picornaviridae* family. Structurally, its genome presents a 5′ noncoding region, a protein-coding region, and a 3′ noncoding region (1). The protein-coding region can be further divided into the P1 area, encoding all four structural proteins, and P2 and P3, encoding nonstructural proteins, including the 2B protein. 2B proteins of poliovirus, coxsackievirus, and other picornaviruses (PVs) have been extensively studied. These 2B proteins contain two hydrophobic regions, and they can insert themselves into the membrane of the endoplasmic reticulum (ER) or the Golgi apparatus to modify cellular membrane permeability once they are expressed in host cells (2–4). Additionally, these 2B proteins can disrupt the Ca^{2+} balance in host cells, affecting apoptosis (5, 6). However, few reports are available on the 2B protein of FMDV. It has been reported that the predicted structure of FMDV 2B contains two hydrophobic regions and inserts itself into the membrane of the ER with its N and C termini oriented toward the cytosol. The same report indicated that the 2B protein increases membrane permeability and can increase the Ca^{2+} content in host cells, thereby inducing autophagy (7).

Here, we report a biochemical and functional characterization of FMDV 2B using different approaches, including an *in vitro* model of artificial membranes. Results revealed that the 2B protein possesses a robust ion channel-forming capacity and, uniquely among other viroporins, possesses two different structural areas that are able to independently mediate pore formation. Consistent with their functional role, these sequences folded as transmembrane helices that were oriented almost perpendicular to the membrane plane. In addition, we present the identification of amino acid residues located in areas harboring pore formation activity, which are critical for the functional activity of 2B and the process of virus replication.

RESULTS

FMDV 2B genomic analysis. FMDV nonstructural protein 2B is encoded within a tract of 462 nucleotides of the FMDV genome, characterized as highly conserved as 2B has one of the lowest percentages of nucleotide substitutions, with only 39% of nucleotide positions and 24% of amino acids being able to tolerate some change. Its nucleotide composition has the most conservative transition (Ts)-versus-transversion (Tv) rate of all FMDV genomic regions (Ts/Tv rate of 6.67), which is even higher than the Ts/Tv rate of the 3D polymerase (Ts/Tv rate of 5.53), indicating the strong constriction to admit significant structural modifications of the RNA (8). Genomic evidence indicates that most of the nucleotide changes are allowed only because they produce a combination that results in the same or very similar amino acids, which is measured by the ratio between the numbers of substitutions that code for the same amino acid. The ratio of 2B synonymous (Syn)/nonsynonymous (non-Syn) substitutions is 5, while ratio for 1D (encoding the structural protein VP1) is 1.03, harboring almost as many Syn as non-Syn changes. Similarly, an alignment of the amino acid sequences of the 2B protein from more than 103 isolates (8) representing all seven serotypes demonstrates that the total number of differences between any two given isolates was never more than 19 substitutions. No matter the origins, host adaptation histories, or antigenic profiles of the pair of viruses compared, there is a remarkably narrow repertoire of possible amino acid compositions for the whole protein, measured as a pairwise identity in 2B of between 81% and 91% (compared with 48% to 68% in 1D), and when a change occurs, it is always a very conservative change. Therefore, FMDV 2B is a 154-amino-acid protein containing 117 invariant residues (Fig. 1A), with amino acid substitutions being limited to only one or two alternate residues per site. This similarity of sequences for the 2B protein across all genotypes and serotypes suggests that its structure and base composition have a critical and specific role in the process of virus replication. The hydrophobicity distribution along the sequence suggested three possible hydrophobic regions that are likely able to form an α-helix that could be part of a transmembrane domain corresponding to amino acids 60 to 78, 84 to 104, and 121 to 141, depicted as red blocks (Fig. 1B). With this information, we defined a collection of overlapping

A.

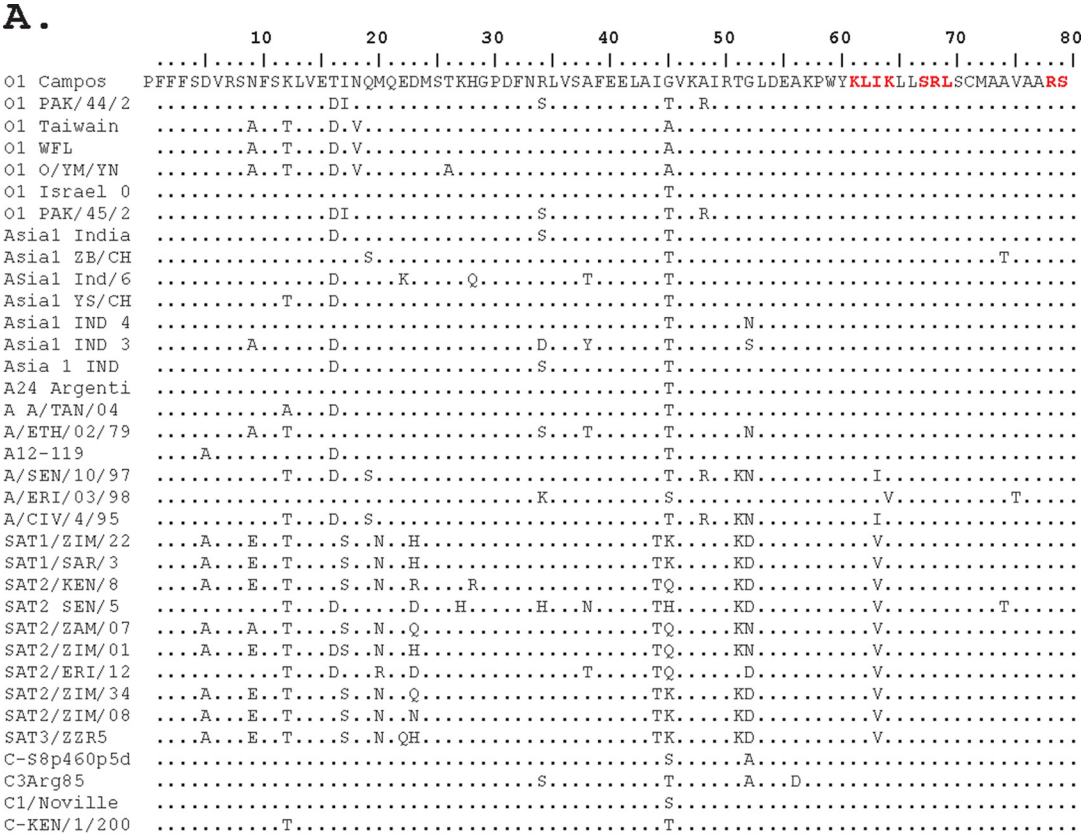

FIG 1 (Continued)

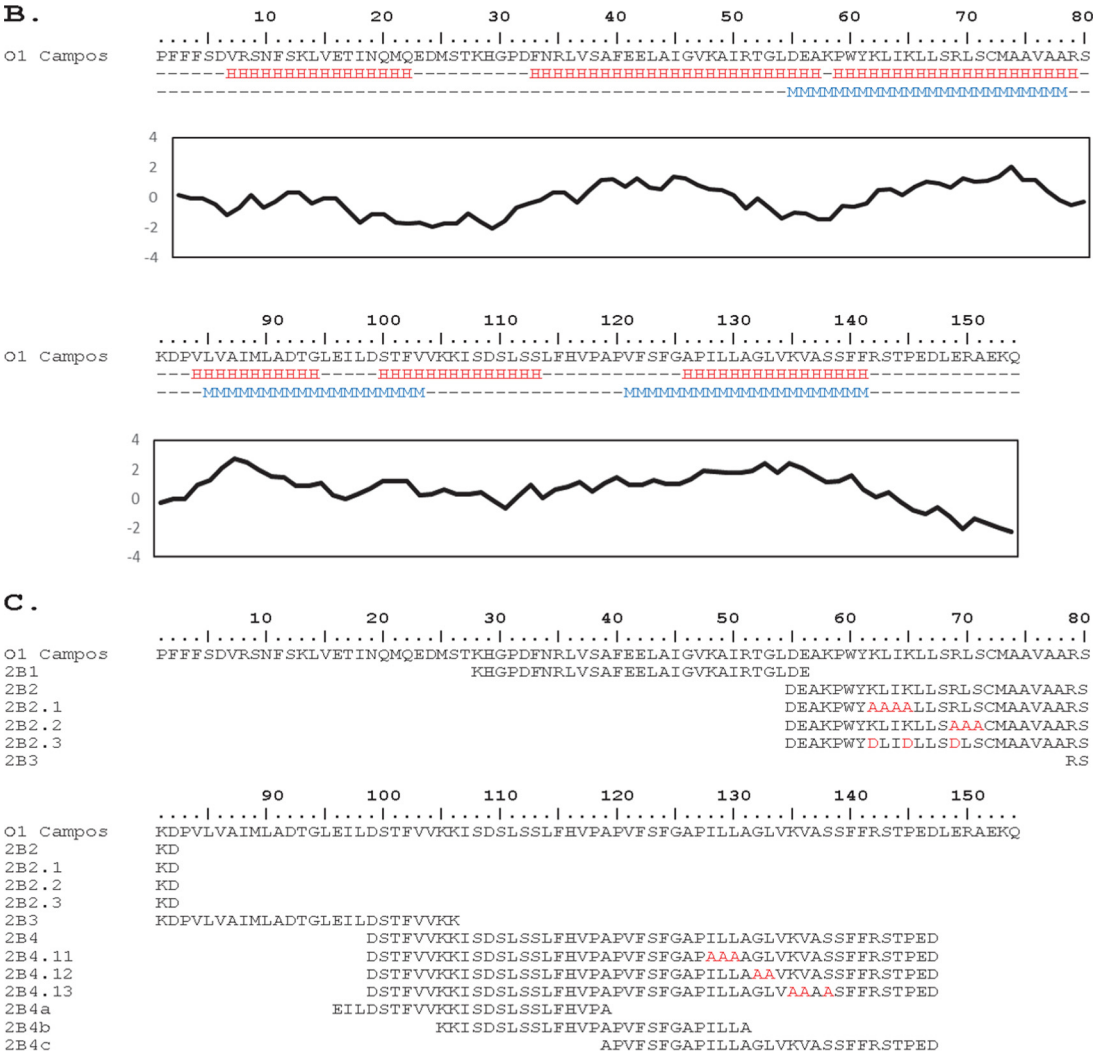

FIG 1 (A) Comparative multisequence alignment of multiple FMDV 2B isolates and predicted structural features. Residues conserved among FMDV isolates are shown as dots. Substituted residues described in Table 2 are shown in red. (B) Amino acids of O1 Campos were used as a representative sequence to predict secondary structure (H is helical) amphiphilicity (with M showing predicted transmembrane regions), and a Kyte-Doolittle plot is shown. Predictions were done on the ExPASY server (39, 40). (C) The peptides used in this study mapped to the amino acid sequence of 2B from O1 Campos. The indicated residues in red are changes from the original amino acid sequence.

sequences, which included the 2B hydrophobic regions, and generated a library of synthetic peptides (Fig. 1C and Table 1).

FMDV 2B protein possesses ion channel activity. The FMDV 2B protein has been shown to behave as a viroporin regarding its cytotoxic effects upon overexpression in bacteria and its capacity for altering trafficking along early secretory pathways in animal cells, where it also seems to induce intracellular calcium release and autophagy (7). However, membrane permeability measurements investigating its pore formation mechanisms at the molecular level had not yet been performed. To this end, we carried out electrophysiological measurements at the level of single ion channels and membrane permeability determinations in single vesicles, using the peptide library (Fig. 1C and Table 1) spanning areas of FMDV 2B potentially involved in viroporin function.

Results presented in Fig. 2 describe the ion channel activity of the FMDV 2B peptides assayed in planar lipid mixtures that mimicked the composition of ER membranes, namely, zwitterionic phosphatidylcholine (PC) and phosphatidylethanolamine (PE) plus anionic phosphatidylinositol (PI) mixed in a roughly 5:3:2 molar ratio (9). Open channels (conductance above the background) were recorded in the cases of the

TABLE 1 ATR-IR data for the FMDV 2B synthetic peptides

Wave no. (cm^{-1})	Vibration[a]	θ (°)[b]	Avg dichroic ratio ± SD	Avg S ± SD[c]	Avg $\gamma^{\perp}$ ± SD[d]	Avg γL ± SD[e]
Lipid alone						
2,920	*as* CH_2 stretching	90	1.94 ± 0.01	0.04 ± 0.01	53.19 ± 0.24	
2,850	*s* CH_2 stretching	90	1.75 ± 0.02	0.16 ± 0.01	48.49 ± 0.53	
2,870	*s* CH_3 stretching	0	3.97 ± 1.00	0.31 ± 0.10	42.44 ± 3.95	
2B1						
2,920	*as* CH_2 stretching	90	1.53 ± 0.07	0.32 ± 0.05	42.41 ± 2.04	
2,850	*s* CH_2 stretching	90	1.40 ± 0.04	0.42 ± 0.04	38.24 ± 1.42	
2870	*s* CH_3 stretching	0	3.73 ± 0.33	0.33 ± 0.04	42.08 ± 1.63	
1656	Amide I–α-helix	30	1.93 ± 0.04	−0.04 ± 0.02	56.22 ± 0.89	58.31 ± 2.12
2B2						
2,920	*as* CH_2 stretching	90	1.70 ± 0.03	0.19 ± 0.02	47.35 ± 0.68	
2,850	*s* CH_2 stretching	90	1.57 ± 0.02	0.28 ± 0.01	43.66 ± 0.53	
2,870	*s* CH_3 stretching	0	4.19 ± 0.72	0.36 ± 0.06	40.55 ± 2.57	
1,656	Amide I–α-helix	30	2.44 ± 0.02	0.18 ± 0.01	47.62 ± 0.28	29.08 ± 1.99
2B3						
2,920	*as* CH_2 stretching	90	1.93 ± 0.08	0.04 ± 0.05	52.99 ± 2.02	
2,850	*s* CH_2 stretching	90	1.73 ± 0.04	0.17 ± 0.03	47.98 ± 1.07	
2,870	*s* CH_3 stretching	0	7.54 ± 4.34	0.40 ± 0.15	38.27 ± 6.52	
1,630	Amide I–β-sheet	70	2.50 ± 0.21	−0.37 ± 0.13	90.00 ± 0.00	90.00 ± 0.00
2B4						
2,920	*as* CH_2 stretching	90	1.74 ± 0.03	0.17 ± 0.02	48.23 ± 0.72	
2,850	*s* CH_2 stretching	90	1.66 ± 0.01	0.22 ± 0.01	46.17 ± 0.37	
2,870	*s* CH_3 stretching	0	4.00 ± 0.61	0.34 ± 0.07	41.36 ± 2.73	
1,656	Amide I–α-helix	30	2.05 ± 0.03	0.02 ± 0.01	53.84 ± 0.53	50.71 ± 2.45
2B4c						
2,920	*as* CH_2 stretching	90	1.77 ± 0.03	0.14 ± 0.02	49.09 ± 0.88	
2,850	*s* CH_2 stretching	90	1.66 ± 0.01	0.22 ± 0.01	46.10 ± 0.33	
2,870	*s* CH_3 stretching	0	4.30 ± 1.23	0.37 ± 0.13	40.24 ± 5.22	
1,656	Amide I–α-helix	30	2.41 ± 0.02	0.17 ± 0.01	48.01 ± 0.34	22.42 ± 3.79

[a]Vibrations are presented as symmetric (*s*) or asymmetric (*as*).
[b]θ, direction of the dipole moment associated with the vibration with respect to the direction of the main molecular axis (aliphatic chain or peptide-secondary structure).
[c]S, form factor.
[d]$\gamma^{\perp}$, angle between the direction of the molecular axis and the perpendicular to the crystal plane (similar to the membrane plane).
[e]γL, angle between the direction of the peptide-secondary structure axis and the calculated aliphatic chain axis.

peptides 2B2 and 2B4, spanning residues 55 to 82 and 99 to 147, respectively, with applied voltages of (±)10, 30, 50, and 70 mV, whereas open channels were not detected for 2B1 or 2B3, spanning residues 28 to 56 or 79 to 106, respectively, even with a stronger potential of ±100 mV applied (Fig. 2A).

In addition, traces showing "opening" and "closing" events were observed for planar bilayers treated with 2B2 or 2B4. These current-versus-time traces were subsequently analyzed with Clampfit 10.1 software so that average current values were obtained for the case of the active sequences under an applied voltage of 50 mV. Histograms of the current jump amplitudes of the recorded traces showed that the most frequent events corresponded to single-channel currents of 7 ± 4 and 5 ± 3 pA for 2B2(55–82) and 2B4(99–147), respectively (Fig. 2B), thereby pointing to a single-channel conductance (G) equal to 20 ± 20 pS. This pattern of changes in conductance was unaffected when an equimolar 2B2-2B4 mixture was added to the supported bilayers, suggesting that both peptides work independently (not shown). In principle, channels formed under these conditions should permit the simultaneous transport of water molecules, solvated ions, and even small solutes, such as Alexa-based fluorescent compounds (10). Supporting that assumption, 2B2 and 2B4 also conducted Ca^{2+} ions efficiently across the ER-mimicking lipid bilayer (Fig. 2C).

Membrane permeabilization induced by FMDV 2B protein-derived synthetic peptides. To gain further insight into the mechanism of permeabilization by FMDV 2B

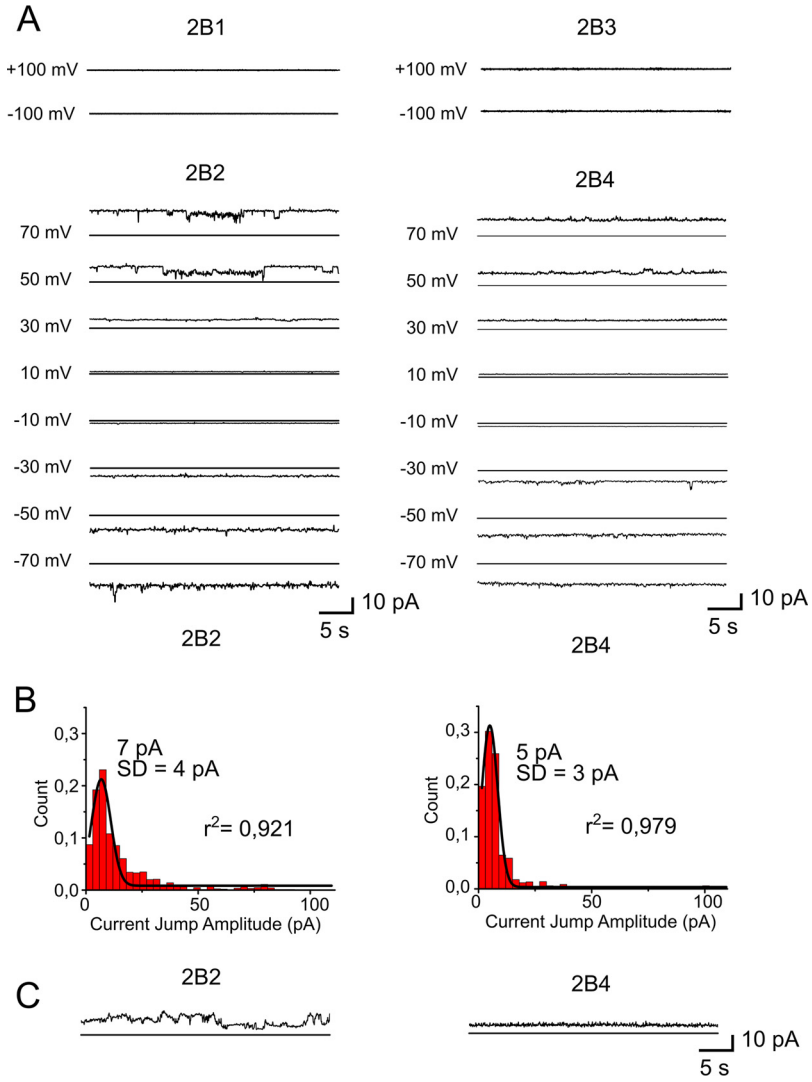

FIG 2 Ion channel activity of 2B peptides. (A) Current recordings in 150 mM KCl, at different potentials, after the addition of 2B1, 2B2, 2B3, or 2B4 to ER-like lipid bilayers. (B) Histograms of the current jump amplitudes recorded for 2B2 and 2B4 with voltage set at 50 mV (left and right panels, respectively). (C) Current recordings measured in 150 mM $CaCl_2$ at 50 mV.

peptides, we complemented ion channel measurements with a single-vesicle approach based on the use of ER-GUVs (Fig. 3A). Confocal micrographs depicted in Fig. 3A compare untreated ER-GUVs (negative control) with those treated with the pore domain of classical swine fever virus viroporin p7 (p7C) (positive control) (11) or the different FMDV 2B peptides. Negative-control vesicles and those treated with the 2B1(28–56) or 2B3(79–106) peptide were viewed as dark (empty) spheres surrounded by the orange-labeled lipid bilayer, against a green background containing the permeant Alexa Fluor 488 dye. In contrast, incubation with the positive control p7C, 2B2(55–82), or 2B4(99–147) resulted in green labeling of the internal ER-GUV compartments, indicating permeabilization of the lipid bilayer to the dye. Overall, these results confirm the pore-forming activity of 2B2(55–82) and 2B4(99–147) sequences, which evolves according to a mechanism that preserves the integrity of the lipid bilayer.

The level of permeabilization (percentage) of a single ER-GUV could be further determined by analyzing the balance of fluorescence intensities inside and outside the vesicle (Fig. 3B). Even though some of the vesicles still showed partial filling at equilibrium, ER-GUVs treated with the 2B2(55–82) or 2B4(99–147) peptide mostly displayed levels of permeabilization approaching 100%. Moreover, the number of

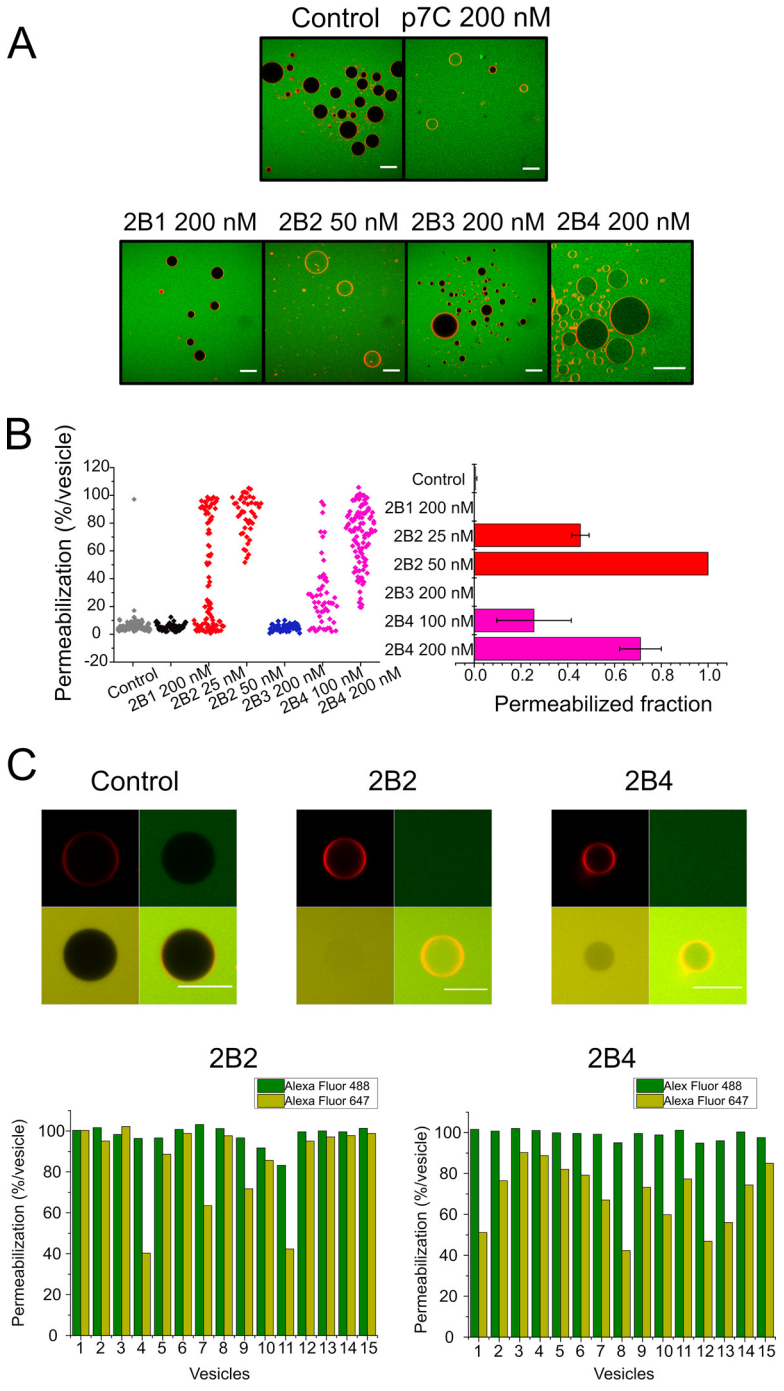

FIG 3 Single-ER-GUV permeabilization induced by 2B peptides. (A) Micrographs depicting Rho-PE -labeled ER-GUVs (orange circumferences) immersed in a solution containing Alexa Fluor 488 (green background). Samples on top correspond to control untreated ER-GUVs (left) or ER-GUVs treated with the p7C peptide derived from CSFV p7 viroporin (11). Bottom samples correspond to ER-GUVs treated with different 2B peptides at the doses displayed on the panels. Bars correspond to 25 μm in all micrographs. (B) Distribution of ER-GUVs according to their percentage of permeabilization to Alexa Fluor 488 after treatment with the different 2B peptides (left) and mean permeabilization values in the samples (right). Peptides were applied at the doses displayed on the panels. (C) Stability of the membrane permeabilization state induced by 2B2 and 2B4. (Top) ER-GUVs permeabilized to Alexa Fluor 488 after incubation for 2 h with 2B2 or 2B4 (green) were supplemented externally with Alexa Fluor 647 (red) and additionally incubated for 2 h before image processing. The presence of both probes inside vesicles can be observed in the merged images (bottom right panels). The "Control" panel displays an intact vesicle incubated in the absence of peptide. (Bottom) Bars represent the degree of filling of individual ER-GUVs with Alexa Fluor 488 (dark green) and Alexa Fluor 647 (light green) after a 4-h incubation with the 2B peptides.

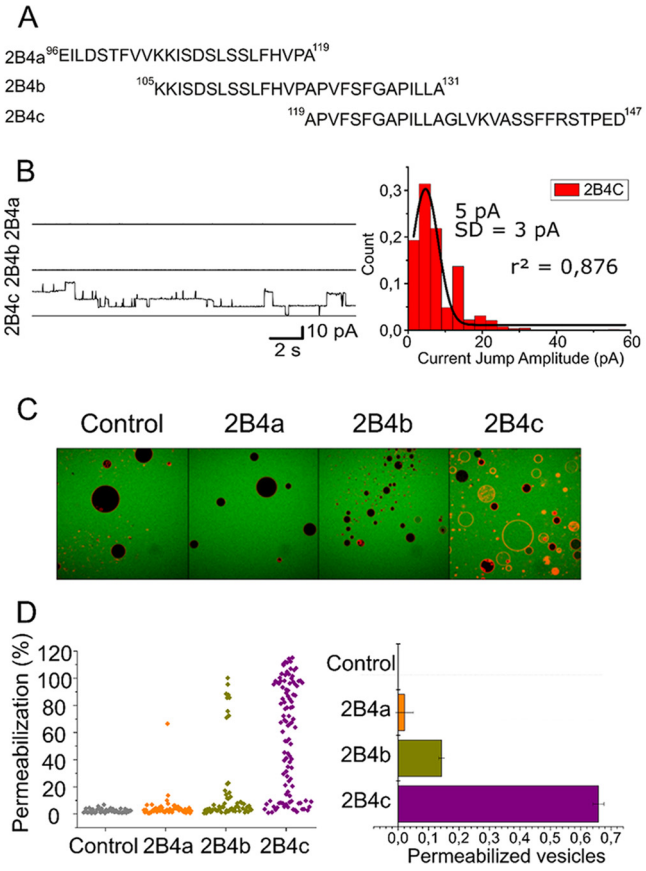

FIG 4 Mapping of membrane-porating activity within the C-terminal end of FMDV-2B. (A) Sequences and range covered by the 2B4-derived overlapping peptides 2B4a, 2B4b, and 2B4c. (B) Ion channel activity of the peptides. Shown are electrophysiological recordings after the addition of 2B4a, 2B4b, and 2B4c (left) and a histogram of current jump amplitudes recorded in lipid bilayers treated with 2B4c (right). Conditions are otherwise as described in the legend of Fig. 2. (C and D) Single-ER-GUV permeabilization. Shown are micrographs of ER-GUVs treated with 2B4-derived peptides (C) and their distributions (D) according to the percentage of permeabilization per vesicle (left) and calculated mean permeabilization values (right). Conditions are otherwise as described in the legend of Fig. 3.

totally permeabilized ER-GUVs increased at the highest doses of peptide tested, but no enhancement was observed for the equimolar 2B2-2B4 mixture (not shown), suggesting again that these domains do not function in a concerted manner. This state of "permanent" permeabilization would be consistent with the above-described ion conductance measurements and supports that ER-GUV permeabilization occurs through pore channels.

To further test this hypothesis, we carried out pore stability assays in which probe diffusion across ER-GUV membranes was measured first with Alexa Fluor 488 and then again with a second dye, Alexa Fluor 647, which was added after a 2-h incubation of vesicles with either the 2B2 or 2B4 peptide (Fig. 3C, top). The permeability to the second dye clearly indicates that vesicles that were permeable to the first dye also allowed the entrance of the second one, demonstrating that most ER-GUVs remain in a permeabilized state, after the first permeabilization event has occurred (Fig. 3C, bottom).

Mapping of pore-forming activity within the region spanning C-terminal residues 99 to 147. The design of the 2B4(99–147) sequence, with an approximate length of 50 amino acids, was performed with the consideration that we did not expect to observe pore activity in this region of the protein. To study in more detail the unexpected activity of this zone, a sublibrary of 3 overlapping peptides was created, 2B4a(96–119), 2B4b(105–131), and 2B4c(119–147) (Table 1 and Fig. 4A), and their

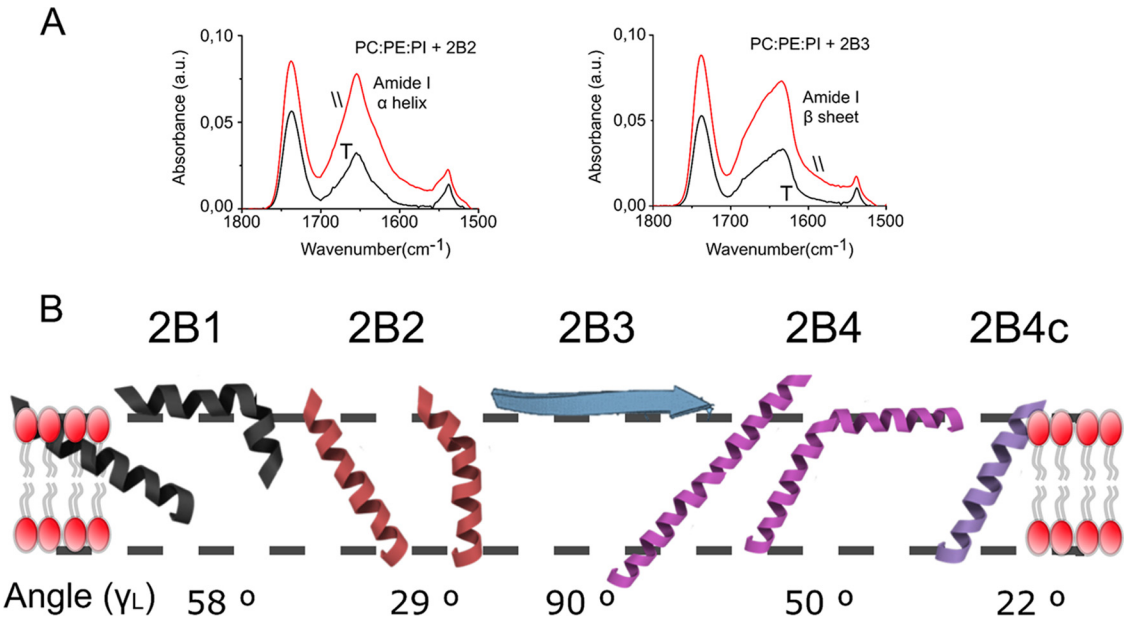

FIG 5 Structures and orientations adopted by 2B peptides in ER-like membranes. (A) Comparison of ATR-IR spectra of 2B2 and 2B3 peptides in the amide I region. Peaks at 1,656 and 1,630 cm^{-1} are indicative of α-helical and extended secondary structures, respectively. The main contained orientation is inferred from the ratio of peak areas recorded with incident light polarized parallel ($\parallel$) and perpendicular ($\perp$) to the membrane normal. a.u., arbitrary units. (B) Models for the orientation of the membrane-associated structures adopted by 2B-derived peptides, which are based on the values of the order parameters and tilt angles displayed in Table 1. Models considering single, continuous helices are accompanied by models considering kinked helical structures.

channel and pore activities were subsequently compared. The data clearly demonstrate that peptide 2B4c(119–147) possesses channel activity with characteristics similar to those of the complete 2B4(99–147) sequence (Fig. 4B). Also, 2B4c(119–147), but not 2B4a(96–119) or 2B4b(105–131), was able to permeabilize ER-GUVs to the Alexa Fluor 488 dye (Fig. 4C). Therefore, it can be concluded that the C-terminal sequence spanning amino acids 119 to 147 of the 2B FMDV protein displays functional characteristics compatible with those of the pore-forming domains.

Structure and orientation of FMDV 2B protein-derived synthetic peptides interacting with membranes. The structure and orientation adopted by the different FMDV 2B peptides in membranes were analyzed using polarized attenuated total reflection infrared (ATR-IR) spectroscopy (Fig. 5). ATR Fourier transform IR (ATR-FTIR) absorbance spectra were measured for the different peptides using perpendicular and parallel polarized light (Fig. 5A). From the spectra, the experimental average dichroic ratios were determined, and order parameters *S* and tilt angles were calculated accordingly (12, 13) (Table 1).

Figure 5B compiles the structures and orientations deduced for the different 2B peptides in the PC-PE-PI lipid bilayer. The spectra of 2B1, 2B2, 2B4, and 2B4c in the amide I region showed single peaks at ca. 1,656 cm^{-1}, compatible with the adoption of a helical conformation for the inserted peptides. In contrast, 2B3 displayed main absorption at 1,630 cm^{-1}, indicative of predominant extended conformations, which seemed unable to insert into the lipid bilayer. Moreover, whereas the 2B1 helix inserted with an orientation of approximately 60° relative to the membrane plane normal, angles of insertion deduced for 2B2, 2B4, and 2B4c were consistent with orientations more perpendicular to the bilayer surface. Since the calculated values of the tilt angles represent average values of the angles in the helix population, the diagram also includes alternative models which consider the possibility of helix sections inserted with different angles and separated by elbows.

FMDV 2B viroporin function is essential for virus growth. To assess the importance of the integrity of the area between amino acid residues 28 and 147 of 2B, using

TABLE 2 Description of amino acid substitutions in the 2B mutant constructs

Location in 2B structure (residues)	Description of amino acid substitution	Name of construct	Name of peptide
Wild type	None	2B.WT	
Helix 1 (60–78)	^{62}KLIK^{65} → ^{62}AAAA^{65}	^{62}KLIK^{65}	2B2.1
	^{68}RLS^{70} → ^{68}AAA^{70}	^{68}RLS^{70}	2B2.2
	^{63}K/^{65}K/^{68}R → ^{63}D/^{65}D/^{68}D	^{63}K/^{65}K/^{68}R	2B2.3
Connection (79–83)	^{79}RSKDP^{83} → ^{79}AAAAA^{83}	^{79}RSKDP^{83}	
	^{79}RS^{80} → ^{79}AA^{80}	^{79}RS^{80}	
	^{83}P → ^{83}A	^{83}P	
Helix 2 (84–104)	^{89}ML^{90} → ^{89}AA^{90}	^{89}ML^{90}	
	^{92}DTG^{94} → ^{92}AAA^{94}	^{92}DTG^{94}	
	^{99}DSTF^{102} → ^{99}AAAA^{102}	^{99}DSTF^{102}	
	^{92}N/^{96}Q/^{99}N → ^{92}Lys/^{96}Lys/^{99}Lys	^{92}N/^{96}Q/^{99}N	
Helix 3 (121–141)	^{128}ILL^{130} → ^{128}AAA^{130}	^{128}ILL^{130}	2B4.11
	^{132}GL^{133} → ^{132}AA^{133}	^{132}GL^{133}	2B4.12
	^{135} KVAS^{138} → ^{135}AAAA^{138}	^{135}KVAS^{138}	2B4.13

reverse genetics, a panel of 13 FMD recombinant mutant viruses was designed, which harbored nonconservative as well as alanine substitutions in critical amino acid residues in this area. A total of 13 cDNA constructs containing the desired amino acid substitutions were designed in the context of a full-length cDNA, pO1C, covering the amino acid residues described in Table 2. The selected residues are situated at one of the three proposed transmembrane regions or in the connecting area between the first two transmembrane regions (Fig. 1). Potential infectious RNAs were *in vitro* transcribed from each of the cDNA constructs and were subsequently used to transfect BHK-21 cells as described in Materials and Methods. Furthermore, to enhance the possibility of rescuing infectious viruses, all transfected cell cultures were further blind passaged six times in LFBK-V6 cells. Infectious virus was rescued from cells transfected using the construct pO1C harboring the wild-type version of 2B (2B.WT). The presence of FMDV cytopathic effect (CPE) was first detected in the second blind passage, becoming extensive by the sixth passage. Virus titers ranged from 4.5 $\log_{10}$ 50% tissue culture infective doses ($TCID_{50}$)/ml in the first passage to 7.0 $\log_{10}$ $TCID_{50}$/ml in the fifth. In contrast, after three independent transfection events, none of the other constructs harboring mutated forms of 2B produced infectious viruses, even after transfection extracts were blind passaged six consecutive times. An exception was constituted by construct ^{83}P, harboring a single P-to-A substitution at residue position 83. Cells transfected with construct ^{83}P showed the presence of cytopathic effect by the fifth blind passage.

The presence of virus RNA, detected by real-time reverse transcription-PCR (rRT-PCR), was analyzed on total RNA extracted from the transfected cells as well as from cells used to perform blind passages. Similar amounts of virus RNA were detected in cells transfected with either the pO1C construct harboring the wild-type version of 2B or constructs corresponding to the 13 2B mutants, suggesting that efficiency of transfection was not responsible for differences in the ability to rescue infectious viruses from the transfected cells (Fig. 6A). The presence of viral RNA (vRNA) decreased in cell extracts obtained from cells used for successive blind passages in all constructs harboring mutated forms of 2B (with the exception of construct ^{83}P, in accordance with the appearance of infectious virus). Conversely, virus RNA in cells transfected with the pO1C (wild-type) construct continued to be detected with each successive cell passage.

Expression of nonstructural protein 2B in cells transfected with the different infectious clone constructs was assessed by Western blotting using a novel anti-2B monoclonal antibody developed by us (Fig. 6B). Expression of 2B in transfected cells was absent regardless of the construct used, including cells transfected with 2B.WT, indicating that under our experimental conditions, protein expression remained undetected in the transfected cells. Similar results were obtained when transfected cells

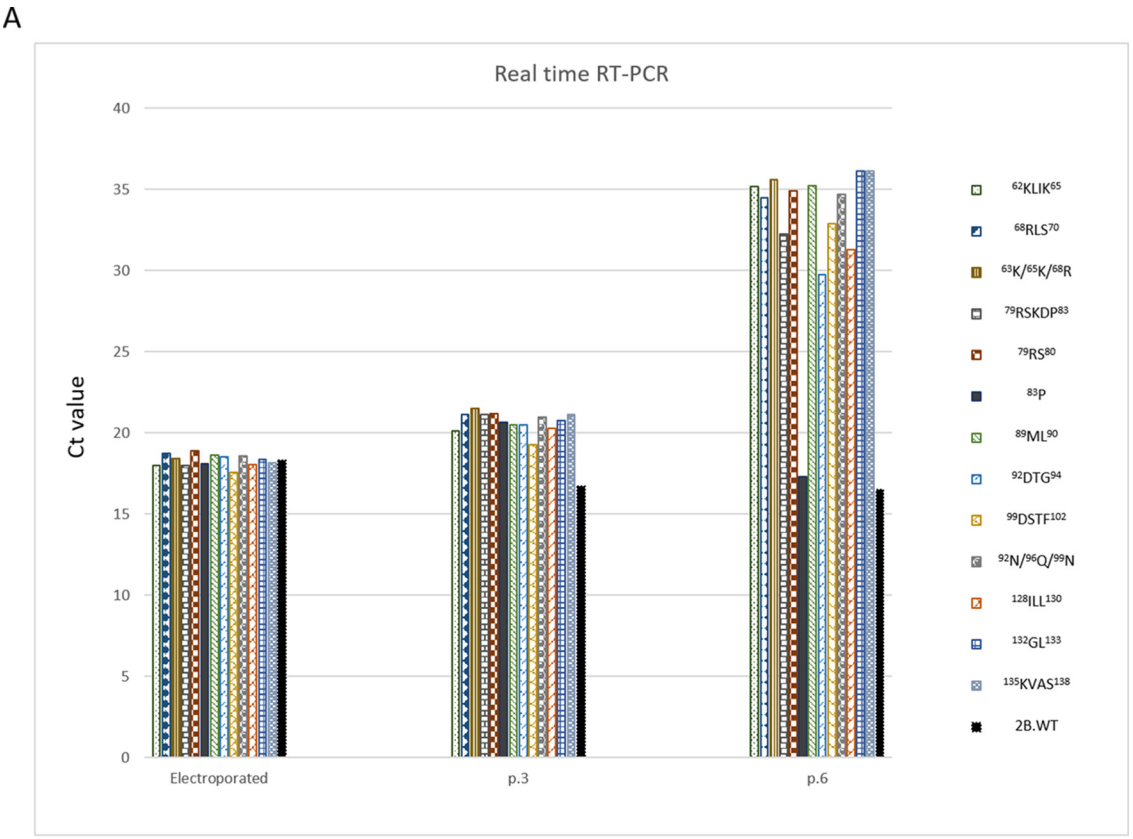

FIG 6 Assessment of the presence of virus replication after transfection. (A) The presence of virus RNA was detected by real-time RT-PCR. Total RNA was isolated from either transfected BHK-21 cells or LFBK-V6 cells used for the third (p.3) and sixth (p.6) blind

(Continued on next page)

were assessed by immunocytochemistry using the same monoclonal antibody (data not show). Western blot analysis of cell extracts from the blind passages demonstrates the consistent presence of 2B in the second passage of cells transfected with 2B.WT or in the fifth passage of cells transfected with construct ^{83}P. Conversely, no 2B expression could be detected in any of the 5 blind passages of any of the other 12 infectious clone constructs harboring mutations in 2B. Analysis of the genomes of viruses rescued after transfection indicated that while no differences were found in the genome encoding the 2B protein in the virus rescued from blind passages of cells transfected with the 2B.WT construct, a reversion to the native sequence (a proline instead of an alanine at position 83) took place in the virus isolated in the fifth blind passage of cells transfected with the ^{83}P construct.

These results confirm that amino acid substitutions in areas of 2B previously characterized as being critical for mediating membrane interactions are also important for virus replication. Amino acid changes in these areas resulted in lethal mutations, halting viral replication.

Effect of lethal mutations on 2B viroporin function. To establish an experimental connection between the viroporin functional assays and the assessment of FMDV replication, we first assessed the effects of the mutations on viroporin activity using variants of the synthetic peptides 2B2 (2B2.1, 2B2.2, and 2B2.3) and 2B4 (2B4.11, 2B4.12, and 2B4.13) (Table 2). None of the 2B2 or 2B4 peptides incorporating the above-described mutations showed channel activity in the electrophysiological recordings (Fig. 7A). In addition, the mutations interfered with the capacity of the peptides to permeabilize ER-GUVs (Fig. 7B).

To confirm the conclusion that the lack of viability of the recombined viruses was caused by the alterations of pore-forming structures, we investigated further the ER localization of the complete 2B protein and the 2B2 and 2B4 mutants expressed in cells (Fig. 7C). Following the pattern previously described to occur in Vero and BHK-21 cells (7, 14), the wild-type fusion protein GFP (green fluorescent protein)-2B colocalized with the ER marker mCh-Sec61 beta in 293T cells. Mutants 2B.1, 2B.3, 2B.11, and 2B.13 displayed significantly lower Pearson colocalization indexes, indicating that alteration of the transmembrane structures interfered with the biogenesis of the 2B protein in these instances. However, 2B.WT and the mutants 2B.2 and 2B.12 targeting 2B2 and 2B4 areas, respectively, colocalized with Sec61 to the same extent, suggesting the correct insertion of these transmembrane variants into the ER membrane of 293T cells.

The identification of these two lethal mutations not interfering with the biogenesis of the protein further allowed establishing their effect on 2B-induced ER permeability to calcium. As displayed in Fig. 8A, compared to cells expressing GFP, the amount of thapsigargin-induced calcium release from the ER was significantly reduced in cells expressing GFP-2B (black and red traces, respectively). Such an effect was consistent with the 2B-induced permeabilization state of the organelle with respect to calcium (7). In contrast, the amounts of calcium releasable from the ER were comparable in GFP- and GFP-2B.12-expressing cells, whereas 2B.2-expressing cells exhibited an intermediate effect (Fig. 8A and B). These observations support the involvement of the transmembrane regions 2B2 and 2B4 in the viroporin activity of FMDV 2B and underline that preserving their function is required for viral growth.

Thus, from a structure-function perspective, it appears that mutations RLSxAAA and GLxAA targeting midway residues of helices 1 and 3, respectively, did not alter their insertion into the ER membrane during biogenesis but interfered with the 2B viroporin function. This can be due to the fact that the mean free energy for transfer and the

FIG 6 Legend (Continued)
passages of transfected extracts. Data are expressed as C_T (cycle threshold) values for all infectious clone constructs described in Table 2. (B) Western blot analysis of FMDV 2B protein expression in cell extracts obtained from either transfected BHK-21 cells (1) or LFBK-V6 cells used for the second blind passages of transfected extracts (2). Expression of 2B in five blind passages of cell transfected with construct ^{83}P is shown (3). C+, positive control, which is an extract of cells infected with FMDV O1 Campos.

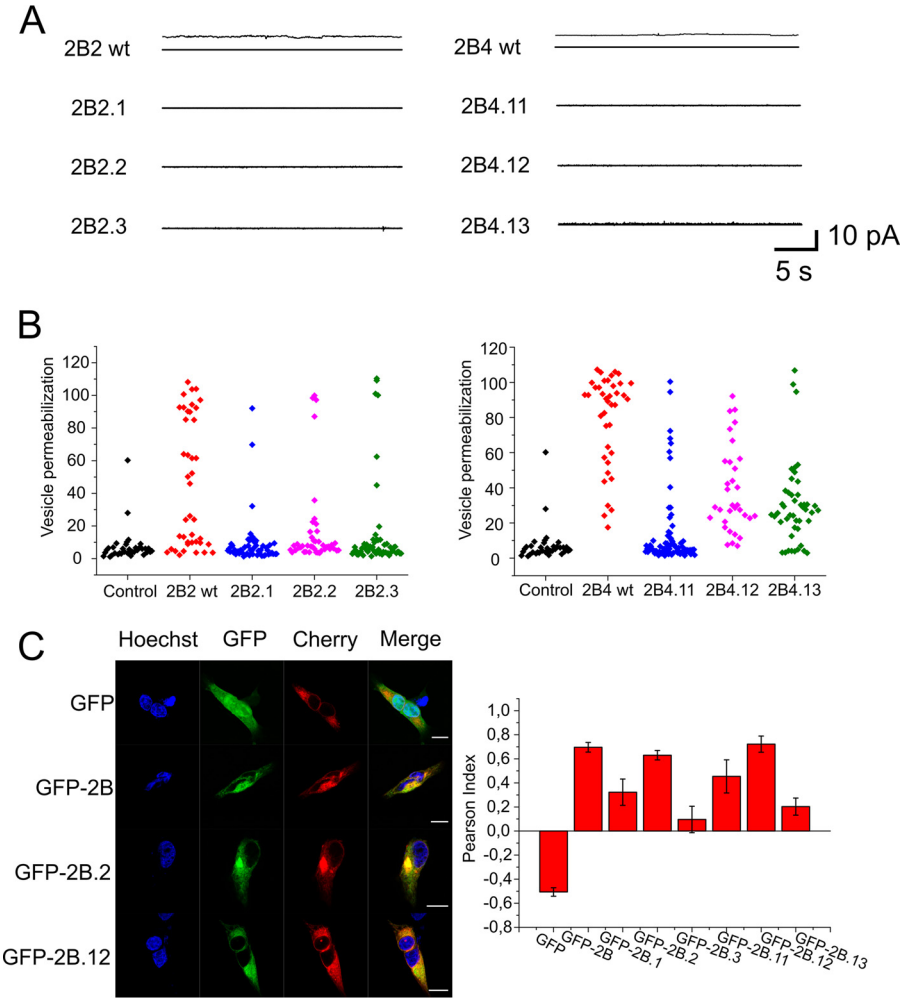

FIG 7 Functional effects of lethal mutations targeting 2B2 and 2B4 transmembrane regions. (A) Current recordings in 150 mM KCl, at a potential of 50 mV, after addition to ER-like lipid bilayers of 2B2 or 2B4 peptide variants incorporating the mutations (recordings on the left and right, respectively). (B) Mean permeabilization values for ER-GUVs treated with 2B2 or 2B4 peptide variants (left and right, respectively). (C) Locations of native and mutated forms of 2B in the ER by confocal microscopy. Micrographs on the left illustrate individual cells coexpressing several GFP constructs and the ER marker mCh-Sec61. Control GFP (i.e., devoid of membrane anchors) labeled the complete cell but was excluded from the ER (top panels), whereas GFP-2B constructs were excluded from the nucleus and colocalized with mCh-Sec61. The panel on the right displays colocalization of mCh-Sec61 and GFP in the samples, including the different 2B mutants, as calculated with the ImageJ plug-in Coloc 2 (http://imagej.net/Coloc_2). Measurements were carried out in at least 6 cells, as for those displayed in the micrograph. Bars represent mean values ± standard errors (SEs). Maximal colocalization with mCh-Sec61 was observed for the fusions, including the 2B.WT protein and the 2B.2 and 2B.12 mutants.

tendency for adopting a defined helical structure were not affected by the Ala residues in these positions. In contrast, replacing the native residues, including the fully conserved R68 and G132 residues (Fig. 1), could be detrimental for the functional assembly of a permeating pore structure.

DISCUSSION

This report focuses on the study of FMDV nonstructural protein 2B, to further characterize its function as a viroporin and its involvement in the process of virus replication. The 2B protein possesses a robust ion channel-forming capacity, and uniquely among other viroporins, it contains two different structural areas able to independently mediate pore formation. These particular areas are folded as transmembrane helices that oriented almost perpendicular to the membrane plane. In addition,

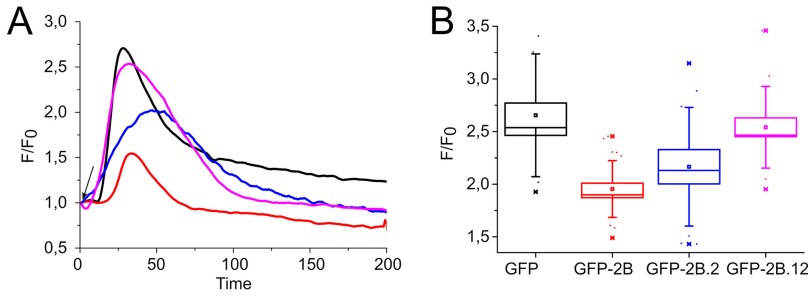

FIG 8 Effects of 2B.2 and 2B.12 lethal mutations on thapsigargin-induced calcium release from the endoplasmic reticulum. (A) Kinetic traces of Ca^{2+} efflux from the ER into the cytosol in cells after thapsigargin addition (final concentration of 10 μM; addition time is indicated by the arrow). Cells were transfected with GFP (black) or the GFP fusions GFP-2B.WT (red), GFP-2B.2 (blue), and GFP-2B.12 (purple). (B) Maximal extents of rhod-2/AM intensity change upon thapsigargin addition to the above-described samples. The analyzed cells transfected with the GFP-2B fusions displayed expression levels comparable to those of the GFP controls. Intensity value distributions were determined for at least 12 single cells, and mean values for the different samples are depicted as box-and-whisker plots (the ends of the whiskers represent SDs).

amino acid residues situated in areas mediating pore formation were shown to be critical in the process of virus replication.

The data obtained using a library of peptides indicate that the 2B sequences spanning residues 60 to 78 and residues 121 to 141 can insert into lipid bilayers as transmembrane helices and form ionic channels or pores, whereas the preceding N-terminal helix is inserted parallel to the plane of the membrane and does not permeabilize the membrane. The structural data for the sequence connecting the two transmembrane helices 1 and 3 were more ambiguous. The observation of a β-like extended structure for the sequence spanning residues 79 to 106, associated with the surface of the bilayer, may reflect a structure similar to that adopted in the context of the complete protein or be consistent with the inability of this sequence to penetrate the core of the acyl chains when disconnected from the preceding transmembrane helix 1 (15, 16).

Thus, based on these results and previous observations that describe the structure-function of 2B from different picornaviruses, we propose two alternative models (Fig. 9). The first model assumes that, similarly to the rest of the picornaviruses (16, 17), the α-turn–α-hairpin motif is applicable to the aphthovirus viroporin 2B (Fig. 9A and B, left). This structural motif implies that the polar interactions between closely spaced helices facilitate their insertion as a single block (15), leaving N and C termini at the same side of the membrane (facing the cytosol in class IIB viroporins [18]). The presence of the basic residues ^{63}Lys/^{65}Lys/^{68}Arg distributed with helical periodicity in helix 1 and the acidic residues ^{92}Asp/^{96}Glu/^{99}Asp in the counterpart helix 2 (Table 2) would support this hypothesis (15). The mutation of these residues proved lethal for FMDV propagation and viroporin activity, indicating that preserving the polarity in these conserved positions is not sufficient for the structure-function of 2B. In addition, maintaining ^{83}Pro, a residue that is preferably selected for as a component of the short turns connecting transmembrane helices (19), is key for viral propagation. Finally, according to this model, a short amphipathic helix spanning residues 102 to 118 could embody the connection between the inserted hairpin and the C-terminal transmembrane helix 3 with the ability to form pores. That is, the C-terminal end of 2B would be positioned facing the ER lumen.

The second model assumes that the N- and C-terminal ends of the 2B protein are oriented toward the cytosol (Fig. 9B, right), as inferred from immunocytochemical analyses (7). According to this model, the pore-forming helices 1 and 3 would be connected through a region associated with the membrane interface that would probably adopt a defined secondary structure (modeled as a continuous helix in Fig. 9B).

The presence of a structural motif found in other 2B proteins of picornaviruses, a

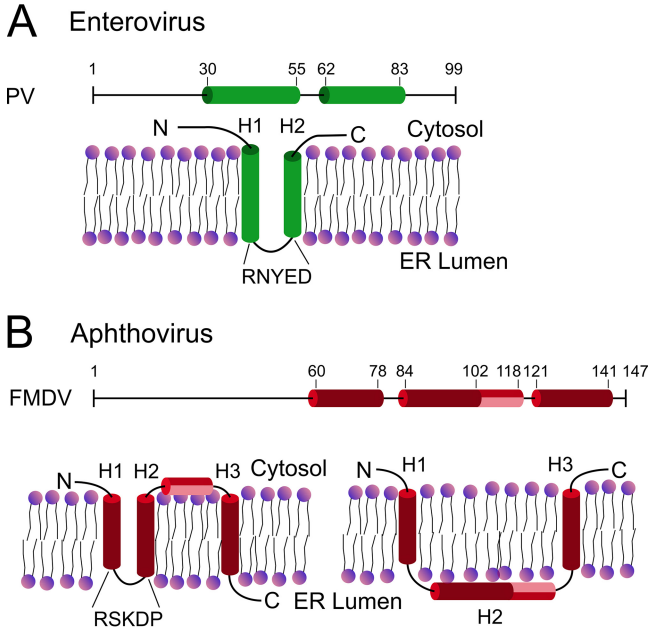

FIG 9 Models for the membrane topologies adopted by viroporins 2B derived from picornaviruses. (A) Enterovirus 2B proteins contain membrane-integral hairpins formed by two poorly hydrophobic helices connected through a short polar turn. (B) Alternative models for FMDV 2B. (Left) Assuming the existence of a membrane-integral hairpin analogous to that of enteroviruses, transmembrane helix 2 (H2) and helix 3 (H3) would be connected through an amphipathic short helix. The C terminus would be facing the lumen of the ER. (Right) Provided that the N and C termini are oriented toward the cytosol, only H1 and H3 would transverse the lipid bilayer.

hairpin formed by poorly hydrophobic transmembrane helices (i.e., difficult to detect by conventional prediction algorithms) connected through a short polar turn, ^{79}RSKDP^{83}, seems to favor the first model over the second one. In this regard, one possibility that cannot be ruled out is that during biogenesis, the insertion of helix 3 does not occur until a time after the proteolytic cleavage that generates 2B and 2C products. That is, in a version of 2B elongated in the C terminus (precursor 2BC or fusion with a hemagglutinin [HA] tag [7]), the insertion of helix 3 could be hindered. It could be speculated that in this situation, the release of a free C terminus after proteolytic processing could allow the insertion of helix 3 at some stage posttranslationally and concomitant with the formation of an oligomeric pore. We emphasize that the hypothetical models in Fig. 9B are not validated by high-resolution structural data and therefore constitute just a speculative interpretation of the data. Taking into account the immunocytochemical data reported by Ao et al. (7), one may speculate further that FMDV 2B encompasses a dual-topology membrane protein, with each orientation endowed with different functions, a feature described for a number of integral membrane proteins (20, 21).

In the present study, we have shown two areas of 2B that independently are capable of forming a pore (helix 1 and helix 3). Pore formation for each of these helices occurs without the presence of additional protein sequence or structure. In view of the existing evidence, we cannot discard the possibility that a structural reorganization of the protein occurs to include both helix 1 and helix 3 domains into a single, perhaps larger, transmembrane channel. Nonetheless, the facts that (i) we do not observe an altered activity for 2B2-2B4 mixtures and (ii) 2B viroporins containing helix 1 domain homologs form transmembrane channels (e.g., PV 2B) in conjunction seem to indicate that the helix 3 domain functions independently of helix 1 in the context of full-length FMDV 2B. Mutations in the infectious clone disrupting critical areas in either of these pore-forming regions were nonviable, suggesting that both pore-forming regions are required for viral growth. This is unique to previously discovered viroporins, where

typically one functional pore is present, and could explain the observation that FMDV 2B proteins contain an insertion and are larger than related enterovirus 2B proteins.

Previous studies of other viruses have shown that in the same virus, two separate individual proteins both form pores. For example, in severe acute respiratory syndrome coronavirus (SARS-CoV), both proteins E and 3A have pore activity, suggesting the possibility that in some cases multiple viroporin functions may be necessary (22, 23). However, for FMDV 2B, further work elucidating the individual functions of either pore will be required to determine the possible different roles for 2B as a viroporin.

MATERIALS AND METHODS

Generation of FMDV 2B mutants. The development of the full-length infectious cDNA clone of FMDV O1 Campos (pO1Ca) was described previously (24). Briefly, the full-length cDNA of O1 Campos was preceded by the T7 polymerase promoter and two additional G residues to improve transcription efficiency and followed by a poly(A) tail of 15 residues and a unique EcoRV site. Plasmid O1Ca containing the desired mutations in 2B was constructed by site-directed mutagenesis. Full-length pO1Ca was used as a template in which native amino acids were substituted by site-directed mutagenesis using the QuikChange XL site-directed mutagenesis kit (Stratagene, Cedar Creek, TX), performed according to the manufacturer's instructions, where the full-length plasmid was amplified by PCR, digested with DpnI to leave only the newly amplified plasmid, transformed into XL10-Gold ultracompetent cells, and grown on Terrific Broth plates containing ampicillin (Teknova, Hollister, CA). Primers were designed by using the manufacturer's primer design program (Agilent).

The obtained full-length infectious clones were completely sequenced with FMDV-specific primers by the dideoxynucleotide chain termination method (25). Sequencing reaction mixtures were prepared with the dye terminator cycle sequencing kit (Applied Biosystems, Foster City, CA). Reaction products were sequenced on a Prism 3730xl automated DNA sequencer (Applied Biosystems). Sequence data were assembled using Sequencher 4.7 software (Gene Codes Corporation, Ann Arbor, MI). The final DNA consensus sequence represented, on average, 3- or 4-fold redundancy at each base position.

Synthetic peptides and lipids. Overlapping 2B sequences of the synthetic peptides displayed in Table 1 were designed by taking into account sequence conservation, hydrophobicity distribution, and the presence of potential turns at the membrane interface, according to procedures described in previous work (3, 26, 27). Synthesis was carried out as previously described (26, 27). Phosphatidylcholine (PC), phosphatidylethanolamine (PE), phosphatidylethanolamine-*N*-(lissamine rhodamine B sulfonyl) (Rho-PE), and phosphatidylinositol (PI) were purchased from Avanti Polar Lipids (Birmingham, AL, USA). Alexa Fluor 488 was obtained from Molecular Probes (Junction City, OR, USA).

Ion channel conductance measurements. Two lipid monolayers were made from 5-mg/ml pentane solutions of a lipid mixture buffered with 5 mM HEPES with KCl (pH 7.4) at both sides of Teflon chambers partitioned by a 15-μm-thick Teflon film with 70- to 100-μm-diameter orifices. Planar lipid bilayers were formed by a monolayer apposition on the orifices previously treated with a 1% solution of hexadecane in pentane. Peptides dissolved in dimethyl sulfoxide (DMSO) were supplemented in the lipid solutions, prior to monolayer formation in only one of the chamber sides, the *cis* side. Bilayer formation was directly detected, and its thickness can be estimated by capacitance measurements. To perform channel conductance measurements, an electric potential was applied using Ag/AgCl electrodes in 2 M KCl–1.5% agarose bridges assembled within standard 250-μl pipette tips. Potential is defined as positive when it is higher at the side of the protein addition (the *cis* side), while the *trans* side is set to ground. The current was amplified by an Axopatch 200B amplifier (Molecular Devices, LLC, Sunnyvale, CA, USA) in the voltage clamp mode (whole-cell $\beta = 1$) with a CV-203BU head stage. Data were digitized with Digidata 1440A (Molecular Devices, Sunnyvale, CA), while the output signal was filtered by an in-line low-pass Bessel filter at 10 kHz and directly saved into the computer memory with a sampling frequency of 50 kHz. The membrane chamber and the head stage were isolated from external noise sources with a double metal screen (custom ordered from Amuneal Manufacturing Corp., Philadelphia, PA, USA). Current amplitude analysis was performed using Clampfit 10.6 software (Molecular Devices, LLC, Sunnyvale, CA, USA). The histograms of the current jump amplitude were made from at least 60 recordings comprising 10 traces with a duration of 20 s, and more than 650 events were analyzed for each histogram. The data were normalized to a value of 1, using the number of total events in each case. The histograms were fitted to a one-peak Gaussian distribution. Each standard deviation (SD) value is the square root variance of the corresponding Gaussian distribution.

Membrane permeability of single vesicles. For the single-vesicle permeability measurements, giant unilamellar vesicles (GUVs) made of PC–PE–PI–Rho-PE (50:30:20:0.1 molar ratio) were prepared according to the electroformation method described in previous works (28, 29). In brief, 2 μl of the ER-lipid mixture (2 mM) was placed on platinum wires, and the solvent was evaporated. For GUV electroformation, 2.4 V and 10 Hz were applied during 2 h in a sucrose (300 mM) solution. To promote detachment of the GUVs from the wires, 2 Hz was finally applied during 30 min. For confocal microscopy analyses, 80 μl of the solution was transferred to 320 μl of buffer (10 mM HEPES, 150 mM KCl [pH 7.4]) in a Lab-Tek eight-chambered number 1.0 borosilicate cover glass from Nalge Nunc International (Rochester, NY, USA), previously blocked with 2 mg/ml bovine serum albumin (BSA).

Confocal fluorescence microscopy images of individual GUVs were obtained using a commercial Nikon D Eclipse TE2000-U fluorescence microscope (Nikon Instruments, Tokyo, Japan). Extents of

permeabilization were calculated for each vesicle after 2 h of incubation with Alexa Fluor 488 and 2B peptides. For this purpose, the fluorescence intensity value outside the vesicle is considered 100%, whereas the intensity inside vesicles reflected the degree of dye diffusion of the percentage of probe entry into the vesicle lumen. Fluorescence emission in the different regions of the sample was quantitated after image processing, and analyses were carried out with ImageJ software (rsb.info.nih.gov/ij/). To assess the stability of the assembled pores, 2 h after peptide-GUV incubation in the presence of free Alexa Fluor 488, a second marker, free Alexa Fluor 647, was added. The entry of both probes into vesicles was analyzed in pictures taken after an additional 2-h incubation.

Attenuated total reflection IR spectroscopy. ATR-IR spectra for the 2B peptides were measured in a Bruker Tensor 27 instrument at a 2-cm^{-1} resolution. PC-PE-PI (5:3:2 molar ratio) lipid mixtures containing peptide (lipid-to-peptide molar ratio, 20:1) were dried on the surface of the ATR Ge crystal by flowing dried air into the infrared spectrometer chamber during 5 h. For spectrum acquisition, a polarized mirror (Pike Technologies) was adjusted to 0° and 90°, to generate incident light oriented parallel and perpendicular to the lipid normal, respectively. A total of 150 IR spectra were collected under each condition and averaged. The dichroic ratio of the amide I bond absorption was computed for parallel (0°) versus perpendicular (90°) polarized incident light relative to the membrane normal and was employed to calculate the peptide orientation as discussed previously (12, 30, 31).

Cell expression and permeabilization of the ER to calcium. ER localization of the expressed 2B protein and its derived mutants was assayed by cotransfecting 293T cells (2×10^5 cells) with plasmids encoding GFP fusions and mCh-Sec61 beta (1 μg each) using calcium phosphate (32). At 36 h posttransfection, cells were fixed with 4% formaldehyde in phosphate-buffered saline (PBS) and incubated with Hoechst dye. Confocal images were acquired on a Leica TCS SP5 II microscope (Leica Microsystems GmbH, Wetzlar, Germany), using a 63× water immersion objective.

2B-induced ER permeabilization was assayed by monitoring the amount of thapsigargin-releasable Ca^{2+} in the cytosol of transfected single cells (33, 34). To this end, changes in the intensity of the indicator probe rhod-2/AM were recorded by fluorescence microscopy as a function of time (35, 36). Thirty-six hours after transfection, cells were loaded with rhod-2/AM (4 μg/ml) at room temperature for 45 min. Dye-loaded cells were visualized with a Nikon Eclipse TE-2000 microscope using a 63× oil immersion objective, after excitation/emission at 561 nm/573 to 613 nm. Thapsigargin was added at a final concentration of 10 μM in culture. Time-lapse images (512 by 512 pixels) of cells displaying 2B-GFP expression levels comparable to those of GFP controls were collected on a Nikon d-Eclipse C1 Si color digital camera (frame acquisition interval of 1 s).

Virus production. Plasmid pO1C or its mutant versions were linearized at the EcoRV site and used as a template for *in vitro* RNA synthesis using the MEGAscript T7 kit (Ambion, Austin, TX) according to the manufacturer's protocols. Attempts to produce genetically modified viruses were performed by transfecting BHK-21 cells (ATCC CCL-10) with *in vitro*-transcribed RNA by electroporation (Electrocell Manipulator 600; BTX, San Diego, CA) as previously described (24). Briefly, 0.5 ml of BHK-21 cells at a concentration of 1.5×10^7 cells/ml in PBS was mixed with 10 μg of RNA in a 4-mm-gap BTX cuvette. The cells were then pulsed once (330 V with infinite resistance and a capacitance of 1,000 F), diluted in cell growth medium (Dulbecco's modified Eagle's medium [DMEM] containing 10% fetal calf serum), and allowed to attach to a T-25 flask. After 4 h, the medium was removed, fresh medium was added, and the cultures were incubated at 37°C for up to 24 h. The supernatants from transfected cells were blindly passaged a minimum of six times or until a cytopathic effect (CPE) appeared in LFBK-V6 cells (a derivative cell line obtained from porcine kidney LFBK cells expressing the bovine V6 integrin) (37).

Western blot analysis. Expression of FMDV nonstructural protein 2B was analyzed in cell lysates of transfected BHK-21 or infected LFBK-V6 cells by Western immunoblotting. FMDV 2B was detected with a monoclonal antibody specifically developed for this work at the Istituto Zooprofilattico Sperimentale della Lombardia e dell Emilia-Romagna, Brescia, Italy. Transfected BHK-21 cells or infected LFBK-V6 cells were harvested using radioimmunoprecipitation assay (RIPA) buffer and the NuPAGE LDS sample buffer system (Invitrogen) and incubated at 70°C for 10 min. Samples were run under reducing conditions in precast Novex 4% to 12% Bis-Tris acrylamide gels (Invitrogen) and transferred to polyvinylidene difluoride (PVDF) membranes (Invitrogen). Goat anti-mouse IgG conjugated to horseradish peroxidase (Pierce, Rockford, IL) was used as a secondary reagent. Western immunoblots were visualized using a SuperSignal West Dura extended-duration substrate (Thermo Scientific) according to the manufacturer's directions. Reactivity was detected with an Azure c300 chemiluminescent Western blot imaging system and cSeries Capture software 2014 (Azure Biosystems).

Detection of viral RNA. Total RNA was isolated from infected BHK-21 and LFBK-V6 cells using an RNeasy minikit (Qiagen, Valencia, CA). Once extracted, vRNA was detected by real-time reverse transcription-PCR (rRT-PCR) on the ABI 7500 system (Applied Biosystems, Austin, TX) as previously described, using specific primers and probe covering the FMDV genomic area encoding nonstructural protein 3D (38).

ACKNOWLEDGMENTS

This research was partially supported by the Basque Government and a University of the Basque Country grant (project IT838-13 to J.L.N.). A.A. and V.M.A. acknowledge financial support from the Spanish Government (FIS2016-75257-P AEI/FEDER) and Universitat Jaume I (P1.1B2015-28).

Also, we especially thank Melanie Prarat for editing the manuscript and Elizabeth Bishop for maintaining and providing LFBK-V6 cells.

REFERENCES

1. Domingo E, Baranowski E, Escarmis C, Sobrino F. 2002. Foot-and-mouth disease virus. Comp Immunol Microbiol Infect Dis 25:297–308. https://doi.org/10.1016/S0147-9571(02)00027-9.
2. de Jong AS, Wessels E, Dijkman HB, Galama JM, Melchers WJ, Willems PH, van Kuppeveld FJ. 2003. Determinants for membrane association and permeabilization of the coxsackievirus 2B protein and the identification of the Golgi complex as the target organelle. J Biol Chem 278:1012–1021. https://doi.org/10.1074/jbc.M207745200.
3. Nieva JL, Agirre A, Nir S, Carrasco L. 2003. Mechanisms of membrane permeabilization by picornavirus 2B viroporin. FEBS Lett 552:68–73. https://doi.org/10.1016/S0014-5793(03)00852-4.
4. van Kuppeveld FJ, Galama JM, Zoll J, van den Hurk PJ, Melchers WJ. 1996. Coxsackie B3 virus protein 2B contains cationic amphipathic helix that is required for viral RNA replication. J Virol 70:3876–3886.
5. Aldabe R, Irurzun A, Carrasco L. 1997. Poliovirus protein 2BC increases cytosolic free calcium concentrations. J Virol 71:6214–6217.
6. Campanella M, de Jong AS, Lanke KW, Melchers WJ, Willems PH, Pinton P, Rizzuto R, van Kuppeveld FJ. 2004. The coxsackievirus 2B protein suppresses apoptotic host cell responses by manipulating intracellular Ca2+ homeostasis. J Biol Chem 279:18440–18450. https://doi.org/10.1074/jbc.M309494200.
7. Ao D, Guo HC, Sun SQ, Sun DH, Fung TS, Wei YQ, Han SC, Yao XP, Cao SZ, Liu DX, Liu XT. 2015. Viroporin activity of the foot-and-mouth disease virus non-structural 2B protein. PLoS One 10:e0125828. https://doi.org/10.1371/journal.pone.0125828.
8. Carrillo C, Tulman ER, Delhon G, Lu Z, Carreno A, Vagnozzi A, Kutish GF, Rock DL. 2005. Comparative genomics of foot-and-mouth disease virus. J Virol 79:6487–6504. https://doi.org/10.1128/JVI.79.10.6487-6504.2005.
9. van Meer G, Voelker DR, Feigenson GW. 2008. Membrane lipids: where they are and how they behave. Nat Rev Mol Cell Biol 9:112–124. https://doi.org/10.1038/nrm2330.
10. Hille B. 2001. Ion channels of excitable membranes, 3rd ed. Sinauer AssociatesSunderland, MA.
11. Largo E, Verdia-Baguena C, Aguilella VM, Nieva JL, Alcaraz A. 2016. Ion channel activity of the CSFV p7 viroporin in surrogates of the ER lipid bilayer. Biochim Biophys Acta 1858:30–37. https://doi.org/10.1016/j.bbamem.2015.10.007.
12. Menikh A, Saleh MT, Gariepy J, Boggs JM. 1997. Orientation in lipid bilayers of a synthetic peptide representing the C-terminus of the A1 domain of Shiga toxin. A polarized ATR-FTIR study. Biochemistry 36:15865–15872. https://doi.org/10.1021/bi970944+.
13. Menestrina G. 2000. Use of Fourier-transformed infrared spectroscopy for secondary structure determination of staphylococcal pore-forming toxins. Methods Mol Biol 145:115–132. https://doi.org/10.1385/1-59259-052-7:115.
14. Moffat K, Howell G, Knox C, Belsham GJ, Monaghan P, Ryan MD, Wileman T. 2005. Effects of foot-and-mouth disease virus nonstructural proteins on the structure and function of the early secretory pathway: 2BC but not 3A blocks endoplasmic reticulum-to-Golgi transport. J Virol 79:4382–4395. https://doi.org/10.1128/JVI.79.7.4382-4395.2005.
15. Bano-Polo M, Martinez-Gil L, Wallner B, Nieva JL, Elofsson A, Mingarro I. 2013. Charge pair interactions in transmembrane helices and turn propensity of the connecting sequence promote helical hairpin insertion. J Mol Biol 425:830–840. https://doi.org/10.1016/j.jmb.2012.12.001.
16. Martínez-Gil L, Bañó-Polo M, Redondo N, Sánchez-Martínez S, Nieva JL, Carrasco L, Mingarro I. 2011. Membrane integration of poliovirus 2B viroporin. J Virol 85:11315–11324. https://doi.org/10.1128/JVI.05421-11.
17. Martinez-Gil L, Mingarro I. 2015. Viroporins, examples of the two-stage membrane protein folding model. Viruses 7:3462–3482. https://doi.org/10.3390/v7072781.
18. Nieva JL, Madan V, Carrasco L. 2012. Viroporins: structure and biological functions. Nat Rev Microbiol 10:563–574. https://doi.org/10.1038/nrmicro2820.
19. Monne M, Nilsson I, Elofsson A, von Heijne G. 1999. Turns in transmembrane helices: determination of the minimal length of a "helical hairpin" and derivation of a fine-grained turn propensity scale. J Mol Biol 293:807–814. https://doi.org/10.1006/jmbi.1999.3183.
20. Rapp M, Granseth E, Seppala S, von Heijne G. 2006. Identification and evolution of dual-topology membrane proteins. Nat Struct Mol Biol 13:112–116. https://doi.org/10.1038/nsmb1057.
21. Woodall NB, Yin Y, Bowie JU. 2015. Dual-topology insertion of a dual-topology membrane protein. Nat Commun 6:8099. https://doi.org/10.1038/ncomms9099.
22. Liao Y, Tam JP, Liu DX. 2006. Viroporin activity of SARS-CoV E protein. Adv Exp Med Biol 581:199–202. https://doi.org/10.1007/978-0-387-33012-9_34.
23. Lu W, Zheng BJ, Xu K, Schwarz W, Du L, Wong CK, Chen J, Duan S, Deubel V, Sun B. 2006. Severe acute respiratory syndrome-associated coronavirus 3a protein forms an ion channel and modulates virus release. Proc Natl Acad Sci U S A 103:12540–12545. https://doi.org/10.1073/pnas.0605402103.
24. Borca MV, Pacheco JM, Holinka LG, Carrillo C, Hartwig E, Garriga D, Kramer E, Rodriguez L, Piccone ME. 2012. Role of arginine-56 within the structural protein VP3 of foot-and-mouth disease virus (FMDV) O1 Campos in virus virulence. Virology 422:37–45. https://doi.org/10.1016/j.virol.2011.09.031.
25. Sanger F, Nicklen S, Coulson AR. 1977. DNA sequencing with chain-terminating inhibitors. Proc Natl Acad Sci U S A 74:5463–5467. https://doi.org/10.1073/pnas.74.12.5463.
26. Gladue DP, Holinka LG, Largo E, Fernandez Sainz I, Carrillo C, O'Donnell V, Baker-Branstetter R, Lu Z, Ambroggio X, Risatti GR, Nieva JL, Borca MV. 2012. Classical swine fever virus p7 protein is a viroporin involved in virulence in swine. J Virol 86:6778–6791. https://doi.org/10.1128/JVI.00560-12.
27. Largo E, Gladue DP, Huarte N, Borca MV, Nieva JL. 2014. Pore-forming activity of pestivirus p7 in a minimal model system supports genus-specific viroporin function. Antiviral Res 101:30–36. https://doi.org/10.1016/j.antiviral.2013.10.015.
28. Apellaniz B, Nieva JL, Schwille P, Garcia SAJ. 2010. All-or-none versus graded: single-vesicle analysis reveals lipid composition effects on membrane permeabilization. Biophys J 99:3619–3628. https://doi.org/10.1016/j.bpj.2010.09.027.
29. Apellaniz B, García-Sáez AJ, Huarte N, Kunert R, Vorauer-Uhl K, Katinger H, Schwille P, Nieva JL. 2010. Confocal microscopy of giant vesicles supports the absence of HIV-1 neutralizing 2F5 antibody reactivity to plasma membrane phospholipids. FEBS Lett 584:1591–1596. https://doi.org/10.1016/j.febslet.2010.03.021.
30. Marsh D. 1997. Dichroic ratios in polarized Fourier transform infrared for nonaxial symmetry of beta-sheet structures. Biophys J 72:2710–2718. https://doi.org/10.1016/S0006-3495(97)78914-8.
31. Goormaghtigh E, Raussens V, Ruysschaert JM. 1999. Attenuated total reflection infrared spectroscopy of proteins and lipids in biological membranes. Biochim Biophys Acta 1422:105–185. https://doi.org/10.1016/S0304-4157(99)00004-0.
32. Zurek N, Sparks L, Voeltz G. 2011. Reticulon short hairpin transmembrane domains are used to shape ER tubules. Traffic 12:28–41. https://doi.org/10.1111/j.1600-0854.2010.01134.x.
33. Moise AR, Grant JR, Vitalis TZ, Jefferies WA. 2002. Adenovirus E3-6.7K maintains calcium homeostasis and prevents apoptosis and arachidonic acid release. J Virol 76:1578–1587. https://doi.org/10.1128/JVI.76.4.1578-1587.2002.
34. Treiman M, Caspersen C, Christensen SB. 1998. A tool coming of age: thapsigargin as an inhibitor of sarco-endoplasmic reticulum Ca(2+)-ATPases. Trends Pharmacol Sci 19:131–135. https://doi.org/10.1016/S0165-6147(98)01184-5.
35. Burnier M, Centeno G, Burki E, Brunner HR. 1994. Confocal microscopy to analyze cytosolic and nuclear calcium in cultured vascular cells. Am J Physiol 266:C1118–C1127. https://doi.org/10.1152/ajpcell.1994.266.4.C1118.
36. Homburg S, Visochek L, Moran N, Dantzer F, Priel E, Asculai E, Schwartz D, Rotter V, Dekel N, Cohen-Armon M. 2000. A fast signal-induced activation of poly(ADP-ribose) polymerase: a novel downstream target of phospholipase C. J Cell Physiol 150:293–307.
37. Gladue DP, O'Donnell V, Baker-Bransetter R, Pacheco JM, Holinka LG,

Arzt J, Pauszek S, Fernandez-Sainz I, Fletcher P, Brocchi E, Lu Z, Rodriguez LL, Borca MV. 2014. Interaction of foot-and-mouth disease virus nonstructural protein 3A with host protein DCTN3 is important for viral virulence in cattle. J Virol 88:2737–2747. https://doi.org/10.1128/JVI.03059-13.

38. Callahan JD, Brown F, Osorio FA, Sur JH, Kramer E, Long GW, Lubroth J, Ellis SJ, Shoulars KS, Gaffney KL, Rock DL, Nelson WM. 2002. Use of a portable real-time reverse transcriptase-polymerase chain reaction assay for rapid detection of foot-and-mouth disease virus. J Am Vet Med Assoc 220:1636–1642. https://doi.org/10.2460/javma.2002.220.1636.
39. Drozdetskiy A, Cole C, Procter J, Barton GJ. 2015. JPred4: a protein secondary structure prediction server. Nucleic Acids Res 43:W389–W394. https://doi.org/10.1093/nar/gkv332.
40. Gasteiger E, Gattiker A, Hoogland C, Ivanyi I, Appel RD, Bairoch A. 2003. ExPASy: the proteomics server for in-depth protein knowledge and analysis. Nucleic Acids Res 31:3784–3788. https://doi.org/10.1093/nar/gkg563.